Benson Philip M (Orcid ID: 0000-0003-2120-3280)
Meredith Philip George (Orcid ID: 0000-0003-2193-5342)
Koor Nick (Orcid ID: 0000-0002-6981-7719)

**Fluid-driven tensile fracture and fracture toughness in Nash Point shale at elevated pressure**

**[1]Gehne, S., [2]Forbes Inskip, N.D., [1]Benson, P.M., [3]Meredith, P.G., and [1]Koor, N.**

[1] Rock Mechanics Laboratory, School of Earth and Environmental sciences, University of Portsmouth, PO1 3QL, U.K.

[2] Lyell Centre, Heriot-Watt University, Edinburgh, EH14 4AP, UK

[3] Rock and Ice Physics Laboratory, Department of Earth Sciences, University College London,      Gower Street, London, WC1E 6BT, U.K.

Corresponding authors: Philip Benson (philip.benson@port.ac.uk) and Nathaniel Forbes Inskip (n.forbes_inskip@hw.ac.uk)

**Key Points:**

- Fracture toughness of an anisotropic shale is calculated using direct fluid pressurization and tensile fracture growth.

- Our data suggest that fracture toughness maintains a consistent value as pressure-driven cracks extend across the sample.

- Fracture toughness increases with confining pressure, and is noticeably higher for fractures crossing bedding planes (Divider orientation) than for those parallel to bedding (Short-Transverse orientation).

**Abstract**

A number of key processes, both natural and anthropogenic, involve the fracture of rocks subjected to tensile stress, including vein growth and mineralization, and the extraction of hydrocarbons through hydraulic fracturing. In each case, the fundamental material property of mode-I fracture toughness must be overcome in order for a tensile fracture to propagate. Whilst measuring this parameter is relatively straightforward at ambient pressure, estimating fracture toughness of rocks at depth, where they experience confining pressure, is technically challenging. Here, we report a new analysis that combines results from thick-walled cylinder burst tests with quantitative acoustic emission to estimate the mode-I fracture toughness ($K_{Ic}$) of Nash Point Shale at confining pressure simulating *in-situ* conditions to approximately 1km depth. In the most favorable orientation, the pressure required to fracture the rock shell (injection pressure, $P_{inj}$) increases from 6.1 MPa at 2.2 MPa confining pressure ($P_c$), to 34 MPa at 20 MPa confining pressure. When fractures are forced to cross the shale bedding, the required injection pressures are 30.3 MPa (at $P_c$ = 4.5 MPa) and 58 MPa ($P_c$ = 20 MPa), respectively. Applying the model of Abou-Sayed (1978) to estimate the initial flaw size, we calculate that this pressure increase equates to an increase in $K_{Ic}$ from 0.36 to 4.05 MPa.m$^{1/2}$ as differential fluid pressure ($P_{inj}$ - $P_c$) increases from 3.2 to 22.0 MPa. We conclude that the increasing pressure due to depth in the Earth will have a significant influence on fracture toughness, which is also a function of the inherent anisotropy.

**1. Introduction**

Hydraulic fracture propagation in the Earth's crust controls many geological processes, both natural and anthropogenic. The development of most unconventional hydrocarbon reservoirs, as well as many geothermal energy reservoirs (particularly engineered geothermal systems), are reliant on the formation of fracture networks created from hydraulic stimulation. Effective rock fracture during drill and blast operations require fractures to extend and interconnect to break the rock, the injection fluid here being a gas rather than a liquid. As such, in order to understand these processes, it is important to understand how the stress conditions with increasing depth in the crust affect the fracture mechanics of the rock, particularly in tension. Aside from environmental parameters such as the *in-situ* stress, pore fluid pressure, and the fluid pressure at the moment of fracture, or breakdown pressure (Warpinski & Smith 1990), a number of key material parameters are also involved in hydraulic fracturing. These include

tensile strength, which determines the stress at fracture initiation, and tensile (mode-I) fracture toughness, $K_{Ic}$, which describes the stress needed to extend a fracture (e.g. Forbes Inskip *et al.,* 2018). Whilst it is relatively straightforward to calculate or measure confining pressure, fluid pressure, and temperature with depth, data on how these parameters influence $K_{Ic}$ with increasing depth is sparse.

This is important, as knowledge of any change in fracture toughness with pressure has direct implications for both natural and engineered processes that involve the evolution of fracture networks in the upper crust. Specifically, pressure increases with depth and is expected to close and reduce the effective length of pre-existing flaws and cracks in rocks, and hence lead to an increase in $K_{Ic}$ (Atkinson, 1979; Meredith and Atkinson, 1985; Atkinson and Meredith; 1987). This is generally what has been observed in the relatively small number of studies to date that have reported the effect of pressure on $K_{Ic}$ (Perkins & Krech 1966; Schmidt & Huddle 1977; Balme *et al.*, 2004; Funatsu *et al.*, 2004; Kataoka *et al.*, 2017). These approaches have generally used 'notched' samples where, under elevated pressure conditions, it is necessary for the pressurizing fluid to enter and fill the notch. However, these techniques suffer from the technical problem of sealing the notch so that the pressurizing fluid cannot enter the propagating fracture, while simultaneously applying a tensile (opening) load. In order to simplify the process, values of $K_{Ic}$ at elevated pressure have been reported either from experimental arrangements where the notch was sealed (e.g. Kataoka *et al.*, 2017) or where the notch was unsealed and the pressurizing fluid was free to enter the propagating fracture. In the latter case, results are not strictly representative of the true $K_{Ic}$ at elevated pressure unless corrected for this discrepancy. Only a small number of studies have attempted to correct for this effect (Kataoka *et al.*, 2017).

We summarize the available data on $K_{Ic}$ at elevated pressure in Figure 1 and tabulate them in detail in Table ST1 (see supporting information). Figure 1 is a synoptic diagram that shows available published values of $K_{Ic}$ at elevated pressure for a wide range of rock types (see supporting information text S1 for additional detail of methods and materials). Here, the elevated pressure $K_{Ic}$ values have all been normalized to their ambient pressure values in order to facilitate comparison between different rock types and thus compare the general effect of elevated pressure. Although the data for individual rock types from individual studies appear to show a systematic increase in $K_{Ic}$ with increasing confining pressure, there does not appear to be any systematic dependence of $K_{Ic}$ on confining pressure when considering the normalized

dataset as a whole. This may be due to inherent differences in the fracture properties of the different rocks, but it may also be the result of a lack of consistency between the different methods used to measure $K_{\text{Ic}}$ under elevated confining pressure conditions.

Driven by this lack of consistency, and the inherent problems associated with sealing notched fracture mechanics samples, we present new data from a novel technique used to calculate $K_{\text{Ic}}$ from tests using internally-pressurized thick-walled cylinder samples (Abou-Sayed, 1978; Gehne *et al.*, 2019).

## 2. Materials and Methods:

Our test material was Nash Point shale. This material is known to be highly anisotropic, and is considered to be representative of the type of mudrocks being targeted as unconventional hydrocarbon reservoir materials (Forbes Inskip *et al.* 2018; Gehne *et al.*, 2019). Nash Point shale is the shaly member of the Porthkerry formation, which is Hettangian-Sinemurian in age and outcrops at Nash Point, South Wales, UK. X-ray Diffraction (XRD) analysis shows that Nash Point shale is composed predominately of calcite (50-70%), with lesser amounts of clay (20-30%) and quartz (10-20%). It has a bulk density of 2,430 kg/m$^3$. A detailed description of the material is given in Forbes Inskip et al. (2018). The mechanical and P-wave anisotropy is 60% and 56%, respectively, as measured from indirect tensile strength tests and radial P-wave velocities (Gehne *et al.*, 2019). It has a porosity of approximately ~6.5%, measured by helium pycnometery, and an intact permeability of approximately 10$^{-18}$ m$^2$ parallel to bedding and 10$^{-20}$ m$^2$ normal to bedding (Gehne and Benson, 2019), also measured using helium gas.

Hydraulic fracturing experiments were carried out in a conventional triaxial deformation cell using cylindrical samples of Nash Point shale 40 mm in diameter and 90 mm in length, with a centrally drilled borehole 12.6 mm in diameter. To account for material anisotropy, samples were prepared with axes either parallel or normal to the bedding planes. The sample assembly is separated from the confining pressure medium using an engineered nitrile jacket fitted with ports for up to 16 measurement sensors (11 acoustic emission (AE) sensors, 1 borehole pressure sensor and 4 radial deformation sensors) (Gehne *et al.*, 2019). The central borehole was fitted with two internal steel guides, sealed with respect to the borehole wall using a number of O-rings (Figure 2). The lower guide was drilled to allow access of the pressurized fracturing fluid to the central sealed-off section of the borehole where it was in direct contact

with the borehole wall over a length of approximately 19mm (the distance between the two innermost O-rings). Unlike some earlier studies (Vinciguerra *et al.*, 2004; Stoeckhert *et al.*, 2015), internal rubber sleeves were not used to separate the fracturing fluid from the rock sample.

To run an experiment, the confining pressure is first applied to a pre-determined level and allowed to equilibrate. Water is then injected at a constant flow rate of 1mL/min into the sealed-off section of the borehole. After approximately 150s, the injection pressure in the borehole starts to increase quasi-linearly. An axial stress is applied to the sample and is set, via servo control, to always slightly exceed the confining pressure or the borehole pressure, whichever is the greatest. This ensures effective sealing of the steel guides throughout the duration of the experiment. Injection pressure increases until it reaches the breakdown pressure, where a hydraulic fracture is initiated at the borehole wall and propagates through the sample thickness. Although a full experiment, including initial pressurization, lasts approximately 1800 s (Figure 3A (inset), and Gehne *et al.*, 2019), the period of interest that spans the peak and post-peak injection pressure behavior spans at most 600 ms. We therefore focus attention on the record of the 500 ms following the peak injection pressure, which is defined to be the 'zero' time. During this time, fracture nucleation and growth is recorded as a rapid decrease in borehole pressure, a rapid increase in the radial deformation of the sample, and an increase in AE activity (Figure 3).

The voltage outputs from 11 AE sensors were passed through coaxial lead-throughs into buffered amplifiers where they were amplified by 30-70 dB (selectable) before being recorded by an AE monitoring system (Itasca-Image Richter). This system also records the voltage output from a dedicated borehole pressure transducer. The system digitizes and records 12 channels of data (11 channels of AE data and 1 channel of borehole injection pressure data) continuously to disk at 10MHz (Fazio *et al.*, 2017) for post experiment processing. The radial deformation of the sample was measured by two cantilever-type radial strain probes attached directly to the sample at 90° to each other using the final 4 jacket ports, with the mean radial strain calculated as $\sqrt{(r_A^2 + r_B^2)}$, where $r_A$ and $r_B$ are the two individual radial strain outputs. These data were recorded on a separate high-speed data acquisition system at 10kHz sampling rate, together with standard axial stress and strain data, and confining pressure.

Recording both the AE and injection pressure data via the high speed (10MHz) AE digitizer ensures that there was no time discrepancy between the different data inputs, with the radial deformation and mechanical data recorded at 10kHz and synchronized via this common injection pressure signal (Gehne, 2018; Gehne *et. al.*, 2019). An example result from an experiment conducted under a confining pressure of 25 MPa is presented as Figure 3. During this experiment, the injection pressure dropped rapidly from 36.5 MPa to 30 MPa at 60ms after peak pressure (zero time in Figure 3). The pressure then recovered to 32 MPa at 65ms before finally decaying slowly over an extended period of time. Many of the other experiments exhibited several of these pressure drop-recovery 'oscillations' between the peak pressure and the final, extended decay period. We suggest that these pressure oscillations occur in response to individual increments of hydrofracture extension. The fracture initially nucleates and extends as the local fracture toughness at the borehole wall is exceeded. This results in a quasi-instantaneous increase in volume and a concomitant rapid decrease in injection pressure. As a result, fracture extension ceases and the injection pressure starts to increase again (recovers) because fluid continues to be injected continuously at the same constant rate. This process can then repeat itself over several pressure oscillation phases, each associated with an increment of fracture extension, until the fracture eventually traverses to the sample boundary. The initial flaw size in the test material ($a_0$), which provides the local stress concentration at the borehole wall from which the fracture nucleates, is calculated using the fracture mechanics model of Abou-Sayed et al. (1978), which is applicable for flaws that are small in relation to the borehole radius (Gehne, 2018), and is given by:

$$P_b = P_c + \frac{K_{Ic}}{1.2\sqrt{\rho a_0}}$$
Eqn. (1)

where: $P_b$ is the breakdown pressure (borehole injection pressure at time of initial tensile failure), $P_c$ is the confining pressure, and $K_{Ic}$ is the fracture toughness.

Thus, the initial flaw size $a_0$ can be determined from the breakdown pressure at zero confining pressure and the ambient pressure fracture toughness of Nash Point shale, which is taken from Forbes Inskip *et al.*, (2018) using either the Short-Transverse value (0.24 MPa.m$^{1/2}$) for the experiments on cores with their long axes parallel to bedding, or the Divider value (0.71 MPa.m$^{1/2}$) for experiments on cores with their long axes normal to bedding (see Figure 4 for explanation of core/fracture orientations).

We now consider the two-stage fracture advance illustrated in the example in figure 3. We use the change in cumulative AE energy (Figure 3B) to estimate the increment of fracture advance during the first pressure drop, and then use this as the starting flaw size for the second pressure fluctuation and second fracture advance. The underlying assumption is that the total cumulative AE energy corresponds to the total fracture advance to the sample boundary. Hence, for the first pressure drop in figure 3, we determine the ratio of the cumulative AE during that pressure drop ($AE_1$) to the total AE energy ($AE_{tot} = AE_1 + AE_2$), and this ratio is equal to the ratio of the fracture extension during that pressure drop $(a_1)$ to the width of the sample shell from the borehole wall to the outer boundary ($r_o$-$r_i$ in Figure 3B). We then use $a_1$ as the starting flaw size for the second increment of fracture advance $(a_2)$ associated with the second pressure drop.  Thus, for each discrete fracture advance and pressure drop we can write:

$$\frac{AE_n}{AE_{tot}} = \frac{a_n}{r_0 - r_i}$$

Eqn. (2)

where $AE_n$ and $a_n$ are the cumulative AE energy and increment of crack extension during cycle $n$, respectively.

We determine the point at which the fracture reaches the sample boundary from the rate-of-change of the fluid injection pressure ($dP_{inj}/dt$). During the initial phase of constant flow prior to any fracture growth, $dP_{inj}/dt$ is constant and low (because the volume injection rate is low at 1 mL/minute). By contrast, during fracture propagation $dP_{inj}/dt$ changes rapidly, decreasing during fracture growth and increasing during pressure recovery (Gehne, 2018). Finally, when the fracture reaches the sample boundary, $dP_{inj}/dt$ again becomes constant and regains the same value as that during the initial constant flow phase. This point occurs at 0.09s in the example illustrated in figure 3. In reality, there is always a time lag between the fracture reaching the sample boundary and the experiment being terminated. During this lag period, the fracture cannot continue to grow radially, but does continue to extend axially by a small amount, resulting in further deformation and AE output.

For each fluid oscillation in experiments where we have multiple oscillation cycles we can then obtain $a_f = \Sigma a_n$, which is the evolving flaw size (cumulative fracture extension) at the start

of each pressure drop. Finally, we can then define a differential pressure ($P_p$ - $P_c$) dependent, or effective, fracture toughness, $eK_{Ic}$, which is calculated from the linear elastic fracture mechanics formulation of Abou-Sayed (1978) via:

$$eK_{Ic} = \left(P_p - P_c\right)\left[F\left(\frac{a_f}{r_i}\right)\sqrt{\rho a_n}\right]$$   Eqn. (3)

where $P_p$ is the peak fluid injection pressure at the start of each pressure drop and increment of crack extension and $P_c$ is the confining pressure. The function $F(a_f/r_i)$ represents the empirical determination of the geometry effect of the thick-walled cylinder (Paris and Sih, 1965), and ranges between approximately 2 for crack increments of 10% of the inner (borehole) radius (in this setup, equivalent to 0.63mm) to unity for propagation across the entire outer shell in one increment (13.7mm, approximately 200% of the inner radius). These functions are tabulated in Paris and Sih (1965), and reproduced in Table ST2 (in the Supporting information) for completeness. For the initial stage, $a_f = a_0$ and the function $F(a_f/r_i)$ is then updated for each subsequent stage with the appropriate value of $a_f$ to allow for an updated calculation of $eK_{Ic}$.

## 3. Results:

A total of 31 experiments were performed across a range of confining pressures and with sample axes cored either parallel or normal to bedding (Gehne, 2018; Gehne *et al.*, 2019). When considering the growth of essentially planar fractures in a material with a planar fabric (such as Nash Point shale), we can define three principal fracture orientations: Short-Transverse orientation, where both the fracture plane and the fracture propagation direction are parallel to bedding; Divider orientation, where the fracture plane is normal to bedding but the fracture propagation direction is parallel to bedding; and Arrester orientation, where both the fracture plane and the fracture propagation direction are normal to bedding (Figure 4). For the thick-walled cylinder geometry used in our experiments, it is only possible to propagate fractures in either the Short-Transverse orientation (for samples cored parallel to bedding) or the Divider orientation (for samples cored normal to bedding). That is because it is always easier for fractures to propagate along the bedding planes rather than across the bedding planes (Arrester orientation) in bedding-parallel cores.

The results from all the experiments are summarized in Figure 5. We selected a subset of 8 experiments from this larger catalogue (Figure 5, solid symbols), and applied the above methodology to compute values of the effective fracture toughness for both Short-Transverse (ST) and Divider (DIV) orientation samples as a function of elevated confining pressure.

Comparing the values of breakdown pressure for the Short-Transverse orientation and Divider orientation samples (Figure 5) reveals that a much higher pressure is needed to fracture the sample in the Divider orientation, with Divider pressures being up to two or three times higher than Short-Transverse pressures for the same value of confining pressure. This is not surprising, since we note that a similar ratio has been reported for the tensile strength and fracture toughness of this material in these orientations when measured at ambient pressure (Forbes Inskip *et al.*, 2018). It is also clear from the data of Figure 5 that the breakdown pressure increases significantly for both orientations with increasing confining pressure.

Figure 6 shows plots of borehole injection pressure, radial deformation and acoustic emission (AE) output against time for three experiments which span the full range of confining pressures used in the study (2.2 MPa, 12.1 MPa and 20.5 MPa). In each case, a sequence of borehole pressure oscillations occurs following the initial breakdown (labelled with numbers on the blue traces in Figure 6), which progressively decrease in amplitude. We note that Short-Transverse samples generally exhibit multiple post-peak pressure oscillations (e.g. Figs. 6A and 6B), whereas Divider orientation samples generally exhibit only a single oscillation (e.g. Fig. 6C). We consider this is likely due to the large differences in fracture energy between the two orientations. The fracture energy release rate in the Divider orientation is an order of magnitude higher than that in the Short-transverse orientation, while the fracture toughness is only about three times higher (Forbes Inskip *et al.*, 2018). Thus, when a fracture nucleates from the borehole wall in the Divider orientation, considerably more stored energy is released relative to the fracture resistance and the fracture is therefore able to propagate much further across the sample before it arrests. We also observe a rapid jump in cumulative AE output (red trace) accompanying breakdown, which then increases steadily throughout the subsequent borehole pressure oscillations. This is accompanied by an inflexion in the radial sample deformation (green trace), further confirming that the initial pressure breakdown marks tensile fracture propagation. However, the largest increases in radial deformation are observed in the final phase of relatively slow pressure decay as the fracture propagates to the sample boundary.

Finally, we note that the breakdown pressure (maximum borehole fluid pressure) increases from approximately 10.4 MPa for the ST orientation test at 2.2 MPa confining pressure, to 27.5 MPa for the ST orientation test at 12.1 MPa confining pressure, and then to 58 MPa for the Divider orientation test at 20.5 MPa confining pressure.

We have applied the analysis described above in section 2 to determine values of $eK_{Ic}$ for each post-breakdown pressure oscillation in each of the eight experiments (five on ST-orientation samples, and three on divider-orientation samples), across the range of confining pressures applied. Wherever we have a pressure oscillation following initial breakdown, we can calculate the differential pressure required for the associated increment of fracture advance ($P_{inj} - P_c$) and the flaw size at the start of that increment of fracture advance. We recorded a total of 17 pressure oscillations in the eight experiments, and this resulted in a total of 17 calculated values of $eK_{Ic}$ over the range of orientations and confining pressures studied which are all listed in Table 1.

We plot all the calculated values of $eK_{Ic}$ from Table 1 as a function of the differential pressure in Figure 7. We observe an essentially linear trend which appears to be independent of sample orientation; with $eK_{Ic}$ increasing from approximately 0.36 MPa.m$^{1/2}$ to 4.05 MPa.m$^{1/2}$ as the differential pressure increases from 1.7 MPa to 22 MPa.

## . Discussion:

There are two key assumptions involved in our determination of the effective fracture toughness of Nash Point shale at elevated confining pressure from fluid injection tests on thick-walled cylinder samples. Firstly, we determine the initial flaw size ($a_o$) in equation 1, for each fracture orientation, using the ambient pressure values of $K_{Ic}$ from Forbes Inskip *et al.* (2018) and assume that it does not vary with confining pressure. This assumption is supported by the data of Chandler *et al.* (2019), where initial flaw sizes were determined from both fluid injection and triaxial deformation experiments for a range of rock types, including two shales (Mancos shale and Whitby mudstone). While the initial flaw sizes for most rocks appeared to decrease with increasing confining pressure, those for the shales remained essentially constant over the confining pressure range 0 to 100 MPa. Furthermore, we also performed a simple sensitivity test of our analysis, whereby we varied the input values of $a_o$ and calculated the effect on the effective fracture toughness ($eK_{Ic}$). We found that varying $a_o$ over an order of

magnitude resulted in a change in $eK_{Ic}$ of less than 1%. We are therefore confident that our reported values of $eK_{Ic}$ are not adversely affected by the initial flaw sizes used in the analysis.

Secondly, we hypothesize that we can accurately estimate the length of fracture advance for each pressure drop during our fluid injection tests from the proportion of the total AE energy generated during that pressure drop. This then provides the starting flaw size for the following pressure oscillation and fracture advance. We consider this hypothesis to be robust in itself, but it is also supported by results and observations from an earlier study of fluid-driven tensile fracturing in thick-walled cylinder samples (Vinciguerra *et al.*, 2004). There, very similar oscillations in injection fluid pressure were observed during post-breakdown fracture propagation, concomitant with similar surges in AE output. However, their observations were also supported by 3D hypocenter location of AE hits that allowed the position of the advancing fracture tip to be determined. These results demonstrated that, for each pressure oscillation, the ratio of the fracture growth associated with that oscillation to the total fracture growth was the same as the ratio of the output of AE energy to the total AE energy. Of course, such an analysis is only accurate if the fractures propagate exactly perpendicular to the sample axis. Post-mortem observation of the fractures generated in both Short-Transverse and Divider orientations demonstrate that fractures do propagate perpendicular to the sample axis (Gehne et al., 2019). This was also the case for the fluid driven fractures reported by Vinciguerra *et al.* (2004) and for fractures in both the Short-Transverse and Divider orientations generated in Nash Point shale during tensile strength and fracture toughness experiments reported by Forbes Inskip *et al.* (2018). Furthermore, where we have multiple pressure oscillations and multiple increments of fracture growth during our fluid injection tests, we are able to make multiple determinations of the fracture toughness, as seen for experiments NPS-ST-2.2, NPS-ST-6.1 and NPS-ST-12.1 in Table 1. We note that all the calculated values of the effective fracture toughness for each of these three experiments are very similar, even though the estimated initial crack lengths increase between oscillation stages. This give us additional confidence in our methodology.

The calculated values of the effective fracture toughness ($eK_{Ic}$) for each pressure oscillation in all eight of our tests are plotted in Figure 8 as a function of confining pressure. These results confirm that the anisotropy in the fracture toughness of Nash Point shale under ambient pressure conditions previously reported by Forbes Inskip *et al.* (2018) is also maintained at elevated confining pressure. The fracture toughness for the Divider orientation is significantly

higher than that for the Short-Transverse orientation for all confining pressures tested. We also observe a general increase in effective fracture toughness with increasing confining pressure in both orientations; with $eK_{Ic}$ increasing to greater than 2 MPa.m$^{1/2}$ in the Short-Transverse orientation and to approximately 4 MPa.m$^{1/2}$ in the Divider orientation at the maximum confining pressure of just over 20 MPa. Extrapolating the Short-Transverse data back to ambient pressure gives a value of 0.22 MPa.m$^{1/2}$, which is very close to the ambient pressure value of 0.24 MPa.m$^{1/2}$ reported by Forbes Inskip *et al.* (2018) for this orientation in Nash Point shale measured using the Semi-Circular Bend methodology (Kuruppu *et al.,* 2014). We are not aware of any reason why the rate of fracture toughness increase with increasing confining pressure should vary with orientation; nevertheless, extrapolating the Divider orientation data back to ambient pressure gives a value that is significantly higher than the ambient pressure value of 0.71 MPa.m$^{1/2}$ reported by Forbes Inskip *et al.* (2018) for this orientation. However, if we compare our data with previously published data for other rock types, we find that, when normalized, they fit well within the spread of values summarized in Figure 1.

When considering the propagation of hydraulic fractures at depth in the Earth, especially anthropogenic fractures propagated to develop hydrocarbon or geothermal energy resources, we note that the majority grow vertically (Fisher and Warpinski, 2012) which, for horizontally-bedded strata, is in the Arrester orientation. It is therefore unfortunate that this is the very orientation that we were unable to access in our experiments. Nevertheless, we note that the fracture characteristics of Arrester orientation cracks and Divider orientation cracks in Nash Point shale tested under ambient conditions were essentially the same (Forbes Inskip *et al.,* 2018); fracture toughness values of 0.74 MPa.m$^{1/2}$ and 0.71 MPa.m$^{1/2}$ in the Arrester and Divider orientations, respectively. This is perhaps not surprising, because the fracture necessarily has to traverse all the bedding interfaces when propagating in either orientation. In the Arrester orientation, all the interfaces are sampled sequentially, while in the Divider orientation they are all sampled simultaneously. We therefore suggest that Arrester orientation fractures are also likely to behave in a similar manner to Divider orientation fractures at elevated confining pressure.

## 5. Conclusions

We have developed a method for deriving the fracture toughness of rock specimens at elevated confining pressure using the conventional thick-walled cylinder geometry (Paris and

Sih, 1965; Zoback *et al.*, 1977; Abou-Sayed *et al.*, 1978; Gehne *et al.*, 2019), using samples of anisotropic Nash Pont Shale (Forbes Inskip *et al.*, 2018). The method takes advantage of the new generation of high speed digitizers for Acoustic Emissions to record the very rapid changes in injection fluid pressure and mechanical (radial) strains associated with fracture opening, and to match changes in AE energy from the crack extension to the changes in injection fluid pressure through time. This has allowed us to calculate a pressure-dependent effective fracture toughness, $eK_{Ic}$.

We find that the internal burst pressure required to fracture samples increases with increasing confining pressure. The burst pressure also depends on the fracture orientation with respect to the bedding planes, as has been widely reported for other anisotropic, layered rocks (e.g. Zoback *et al.*, 1977; Warpinski *et al.*, 2012; Stoeckhert *et al.*, 2015; Li *et al.*, 2016; Forbes Inskip *et al.*, 2018; Gehne *et al.*, 2019). The hydraulic fractures commonly propagate in distinct increments, each associated with an injection pressure oscillation. Each sequential oscillation and fracture growth increment requires a lower differential fluid pressure due to the increasing fracture length.

Finally, we conclude that the effective fracture toughness increases significantly with increasing confining pressure. The anisotropy in fracture toughness observed under ambient conditions (Forbes Inskip *et al.,* 2018) is maintained at elevated confining pressure. For all confining pressures tested, the effective fracture toughness was noticeably higher in the Divider orientation than in the Short-Transverse orientation. This is likely due to the necessity for fractures to cross bedding planes when propagating in the Divider orientation, compared to propagating along the bedding planes when propagating in the Short-Transverse orientation. We consider such data to be of importance in a wide variety of settings, ranging from dyke intrusion to anthropogenic hydraulic fracturing.

https://www.bgs.ac.uk/services/ngdc/accessions
/index.html?simpleText=NE/L009110/1#item131125.


**References**

Abou-Sayed, A., Brechtel, C. and Clifton, R. (1978), In situ stress determination by hydrofracturing: a fracture mechanics approach. J. Geophys. Res. (solid Earth), 83, 2851–2862.

Abou-Sayed, A. (1978), An experimental technique for measuring the fracture toughness of rock under downhole stress condition. VDI-berichte, 313, 819–824.

Atkinson, B. K. (1979), A fracture mechanics study of subcritical tensile cracking of quartz in wet environments. Pure and Applied Geophysics, 117 (5), 1011–1024.

Atkinson, B.K. & Meredith, P.G. (1987), The theory of sub-critical crack growth with application to minerals and rocks. In: Fracture mechanics of rock. San Diego: Academic Press, p.111-166.

Balme, M.R., Rocchi., V., Jones., C., Sammonds, P., Meredith, P, & Boon, S. (2004). Fracture toughness measurements on igneous rocks using a high-pressure, high-temperature rock mechanics cell. J. Volc. Geotherm. Res., 132, 159-172.

Chandler, M. R., Meredith, P. G., Brantut, N. & Crawford, B. R. (2016), Fracture toughness anisotropy in shale. J. Geophys. Res. (solid Earth), 121, 1706–1729.

Chandler, M. R., Mecklenburgh, J., Rutter, E. & Lee, P. (2019). Fluid injection experiments in shale at elevated confining pressures: determination of flaw sizes from mechanical experiments in shale. J. Geophys. Res. (solid Earth), 124, 5500-5520.

Fazio, M., Benson, P. M. and Vinciguerra, S. (2017). On the generation mechanisms of fluid-driven seismic signals related to volcano-tectonics. Geophysical Research Letters, 44 (2), 734–742.

Fisher, K. & Warpinski, N. (2012). Hydraulic-fracture-height growth: Real data. Society of petroleum engineers. doi: 10.2118/145949-PA.

Forbes Inskip, N. D., Meredith, P. G., Chandler, M. R., & Gudmundsson, A. (2018). Fracture properties of Nash Point shale as a function of orientation to bedding. J. Geophys. Res. (solid Earth), 123. doi:10.1029/2018JB015943

Funatsu, T., Seto, M., Shimada, H., Matsui, K., and Kuruppa, M. (2004), Combined effects of increasing temperature and confining pressure on the fracture toughness of clay-bearing

rocks. International Journal of Rock Mechanics and Mining Sciences & Geomechanics Abstracts, 41, 927-938.

Gehne, S. (2018), A laboratory study of fluid-driven tensile fracturing in anisotropic rocks. PhD Thesis, University of Portsmouth. Preprint at https://ethos.bl.uk/OrderDetails.do?uin=uk.bl.ethos.765705.

Gehne, S., Benson, P.M, Koor, N., Dobson, K.J., Enfield, M., and Barber, A. (2019), Seismo-mechanical response of anisotropic rocks under simulated hydraulic fracture conditions: new experimental insights. J. Geophys. Res. (solid Earth), 124, doi:10.1029/2019JB017342.

Gehne, S., & Benson, P.M. (2019), Permeability enhancement through hydraulic fracturing: new laboratory measurements combining a 3D printed jacket and direct over-pressure. Nature Sci. Rep. 9, 12573, doi: 10.1038/s41598-019-49093-1.

Kataoka, M., Eqlima, M., Funatsu, T., Takehara, T., Obera, Y., Fukui, K., & Hashiba, K. (2017), Estimation of mode-I fracture toughness of rock by semi-circular bend test under confining pressure condition. Procedia Engineering, 191, 886-893, doi: 10.1016/jproeng.2017.05.258.

Kuruppu, M.D., Obara, Y., Ayatollah, M.R., Chong K.P., & Funatsu T. (2014) ISRM-suggested method for determining the Mode I static fracture toughness using semi-circular bend specimens. In: R. Ulusay (Ed.), *The ISRM suggested methods for rock characterization, testing and monitoring 2007-2014 (pp. 107-114), Springer, Wien.*

Li, X., Feng, Z., Han, G., Elsworth, D., Marone, C., Saffer, D. and Cheon, D.-S. (2016). Breakdown pressure and fracture surface morphology of hydraulic fracturing in shale with $H_2O$, $CO_2$ and $N_2$. Geomechanics and Geophysics for Geo-Energy and Geo-Resources, 2 (2), 63–76.

Meredith, P.G. & Atkinson, B.K. (1985), Fracture toughness and subcritical crack growth during high-temperature tensile deformation of westerly granite and black gabbro. Phys. Earth Planet. Int. 39, 33–51.

Paris, P. C. & Sih, G. C. (1965), Stress analysis of cracks. In: Fracture toughness testing and its applications, ASTM International.

Perkins T.K. & Krech W.W. (1966), Effect of cleavage rate and stress level on apparent surface energies of rocks, SPE Journal, 6, 308-314.

Schmidt, R.A. & Huddle, C.W. (1977). Effect of confining pressure on fracture toughness of Indiana limestone. International Journal of Rock Mechanics and Mining Sciences & Geomechanics Abstracts, 14 (5-6), 289-293, doi.org/10.1016/0148-9062(77)90740-9.

Stoeckhert, F., Molenda, M., Brenne, S. and Alber, M. (2015). Fracture propagation in sandstone and slate-Laboratory experiments, acoustic emissions and fracture mechanics. Journal of Rock Mechanics and Geotechnical Engineering, 7 (3), 237–249.

Vinciguerra, S., Meredith, P. G. and Hazzard, J. (2004). Experimental and modeling study of fluid pressure-driven fractures in Darley Dale sandstone. Geophysical research letters, 31 (9), L09609.

Warpinski, N., & Smith, M. B. (1990). Rock mechanics and fracture geometry. In J. L. Gidley, S. A. Holditch, D. E. Nierode, & R. W. Veatch, Jr. (Eds.), Recent advances in Hydraulic Fracturing (pp. 57–80). Richardson, TX: Society of Petroleum Engineers.

Warpinski, N. R., Du, J. and Zimmer, U. (2012). Measurements of hydraulic-fracture-induced seismicity in gas shales. SPE Production & Operations, 27 (3), 240–252.

Zoback, M., Rummel, F., Jung, R. and Raleigh, C. (1977). Laboratory hydraulic fracturing experiments in intact and pre-fractured rock. In: International Journal of Rock Mechanics and Mining Sciences & Geomechanics Abstracts, 14 (2), 1977, 49–58.
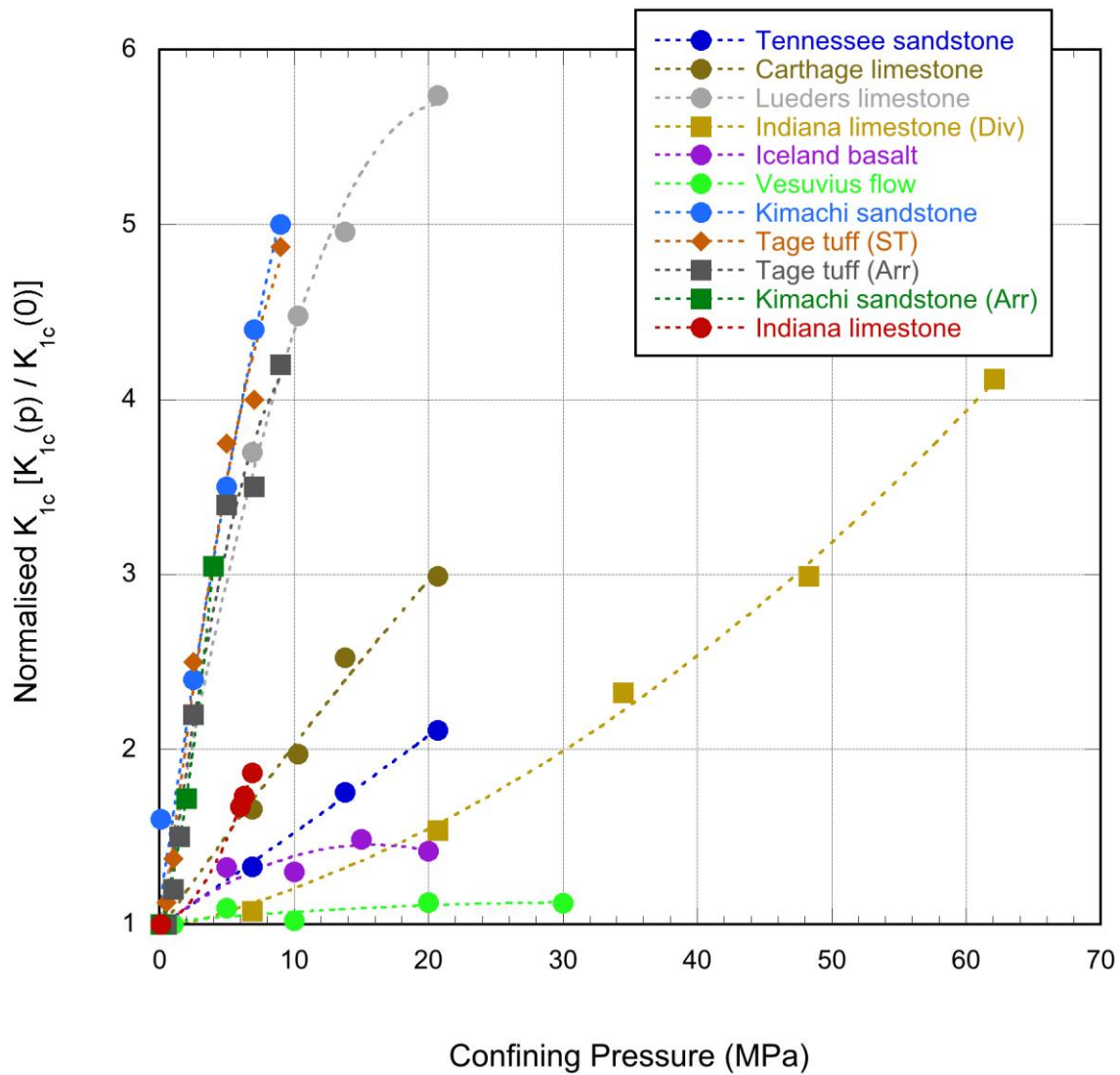
**Figure 1:** Plot of normalised $K_{Ic}$ at different confining pressures for rocks from the studies listed below. Here $K_{Ic}$ measured at pressure ($K_{Ic}$ (p)) is normalised to the value at ambient pressure ($K_{Ic}$ (0)). Further information on each of the studies listed is provided in the supporting information (S1) and table (ST1). (ST), (Arr) and (Div) refer to the principal fracture orientations; Short-Transverse, Arrester and Divider, respectively. Data taken from [1] Perkins & Krech (1966), [2] Schmidt & Huddle (1977), [3] Abou-Sayed (1978), [4] Balme *et al.* (2004), [5] Funatsu *et al.* (2004) and [6] Kataoka *et al.* (2017).
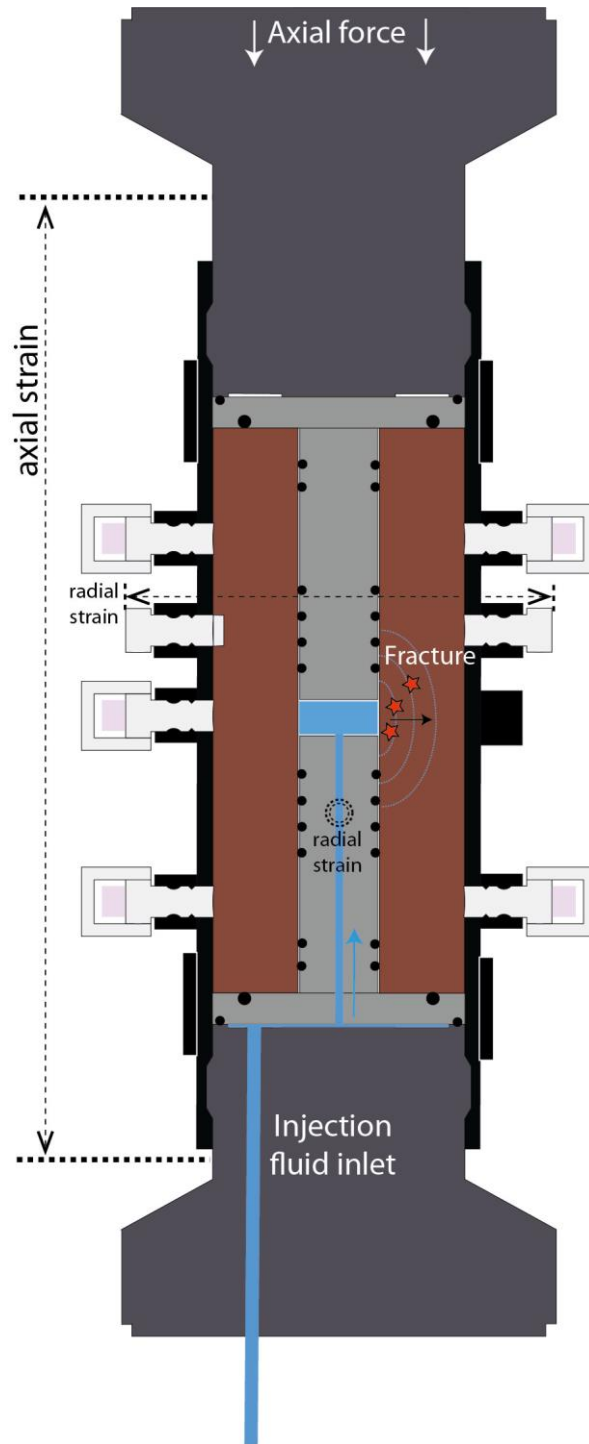
**Figure 1:** Schematic diagram of the sample assembly used in this study. The steel injection fluid guides are fitted with O-rings to isolate the pressurizing fluid (water) from the confining pressure ($\sigma_2 = \sigma_3$). The axial principal stress, $\sigma_1$, is controlled via electronic servo-control to ensure positive sealing throughout the experiment. After Gehne *et al.* (2019).
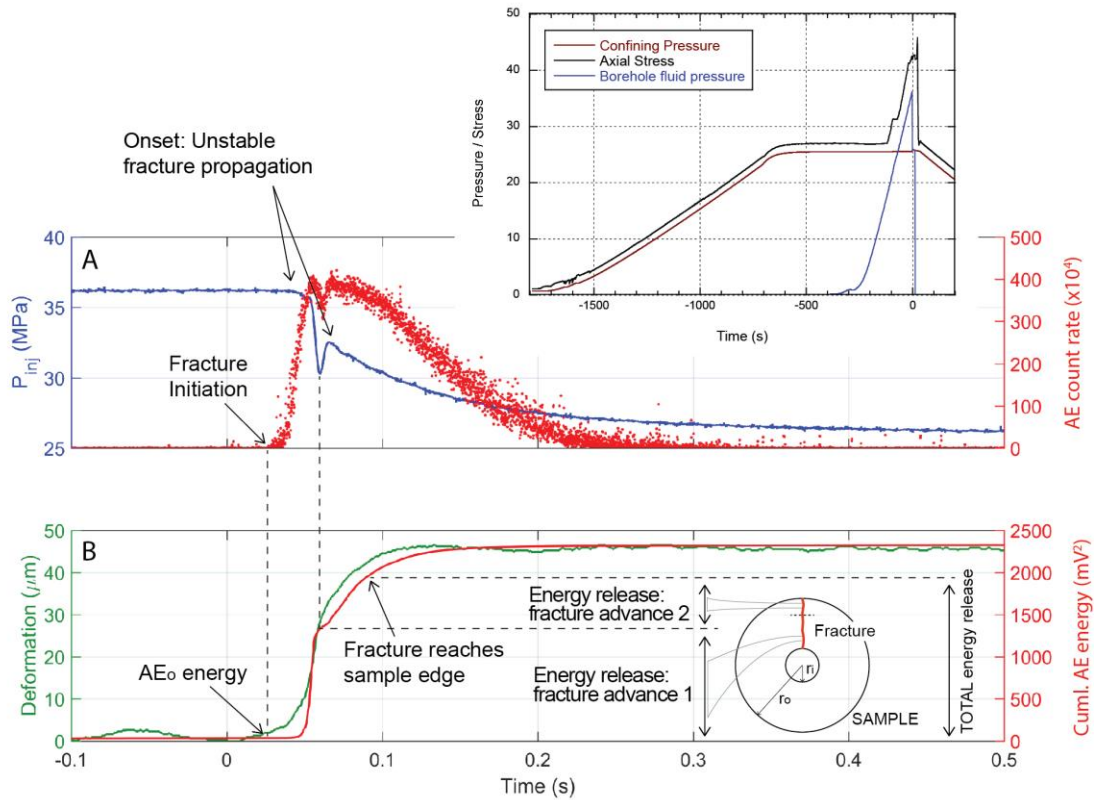
**Figure 3:** Concept of effective fracture toughness calculation from thick walled cylinder experiments at elevated pressures in Nash Point Shale. Top panel and inset: blue trace shows the borehole injection pressure with time, showing a sharp decrease at initial fracture. Simultaneously, a rise in AE count rate (red dots) is measured. Note the high speed of the process over just 600ms: the inset shows a typical full experiment over some 1800s. Lower panel: Replotting the AE as a cumulative energy (red line) allows the determination of the energy required to advance each fracture stage, using the change in borehole fluid pressure as a guide. The sample geometry (lower right sketch) illustrates the energy advance apportioned to each stage of the fracture process, where $r_i$ and $r_o$ are the borehole and sample radii, respectively.
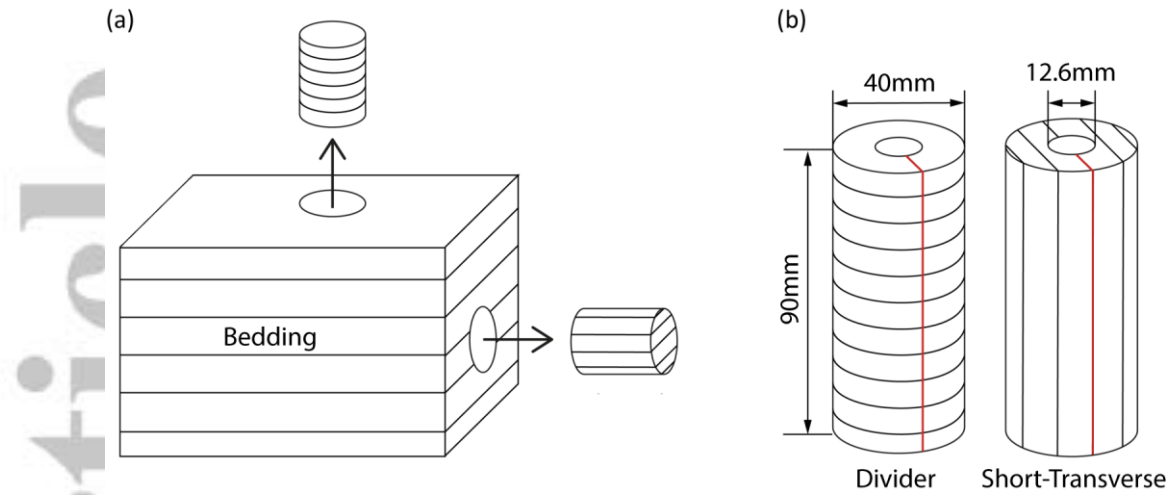
**Figure 4:** Schematic of the bedding/fracture plane relationships as used in this study. Blocks of Nash Point shale as collected in the field (a) exhibit clear sedimentary bedding that is use to defines to orientations for coring of the cylindrical samples. Cores with long-axis normal to bedding are designated as the Divider orientation, with cores with long-axis parallel to bedding designated Short-Transverse (b). Typical failure planes are annotated with red lines.
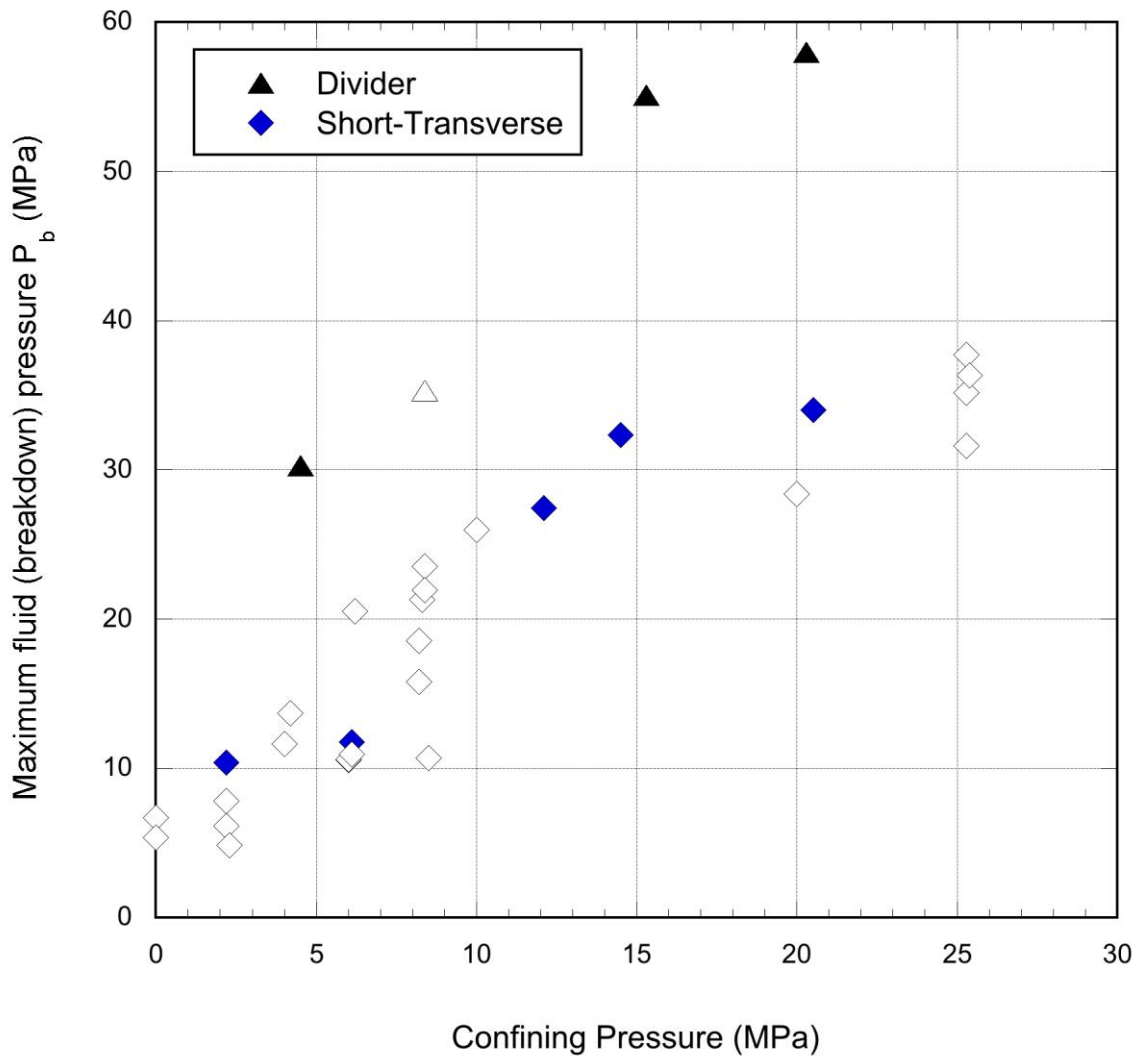
**Figure 5:** Plot of borehole breakdown pressure as a function of confining pressure for all experiments on Nash Point shale from the wider study (after Gehne, 2018). Here, we focus on results from a subset of eight experiment; three in the Divider orientation (solid black triangles) and five in the Short-Transverse orientation (solid blue diamonds). In general, a higher breakdown pressure is required to propagate fractures in samples under higher confining pressure; with Divider orientation samples requiring significantly higher pressure than Short-Transverse samples at the same confining pressure.
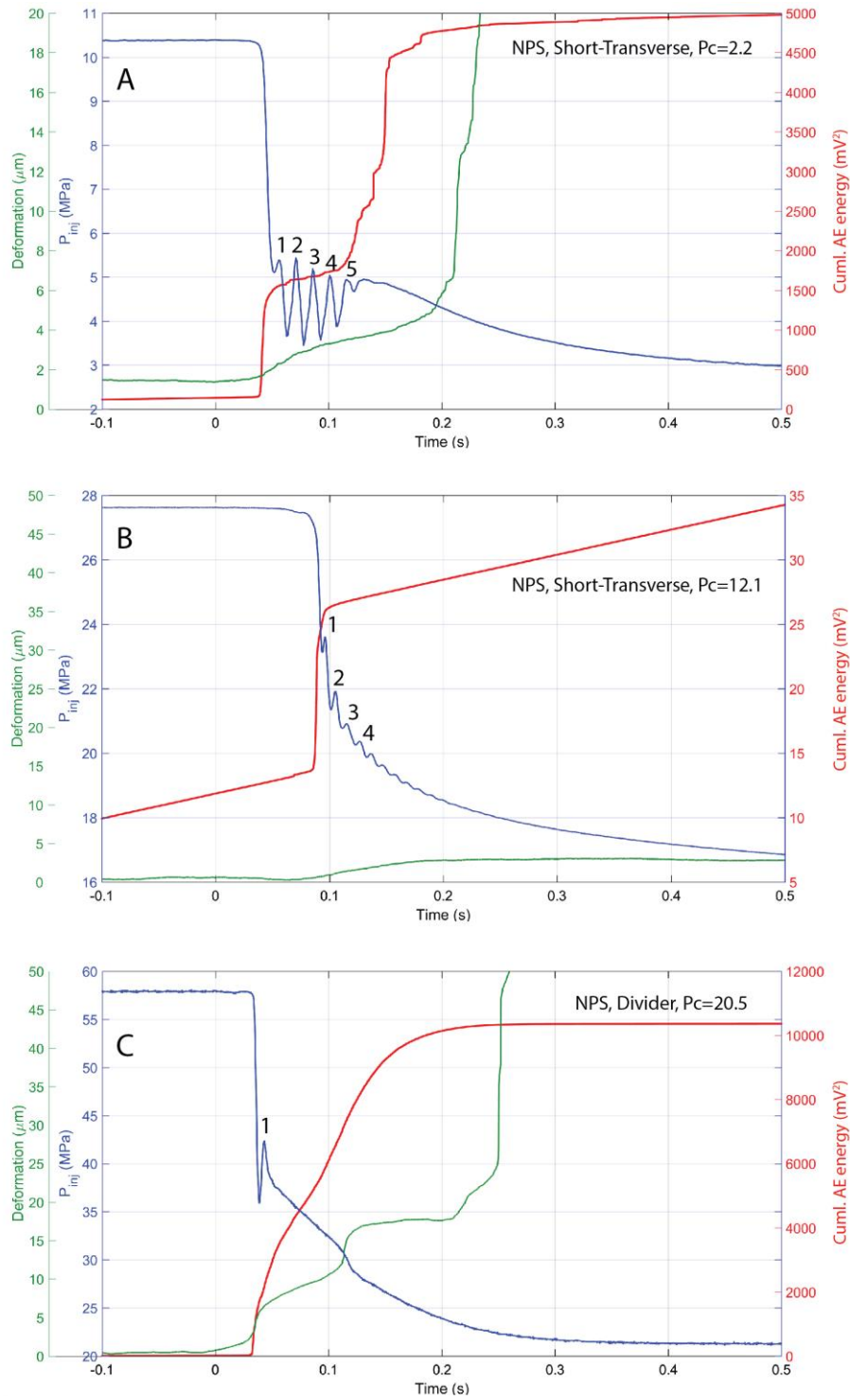
**Figure 6:** Three example datasets for fluid-driven fracture at confining pressures of 2.2 MPa (top), 12.1 MPa (centre) and 20.5 MPa (bottom). In each case the borehole injection pressure (blue traces) drops at the moment of initial tensile failure (breakdown), with both radial deformation (green traces) and cumulative AE output increasing at the same time. The amplitude and number of injection pressure oscillations decreases with confining pressure and time. Analysis points (stages) for calculating values of $eK_{Ic}$ are labelled numerically for each case, and summarized in Table 1.
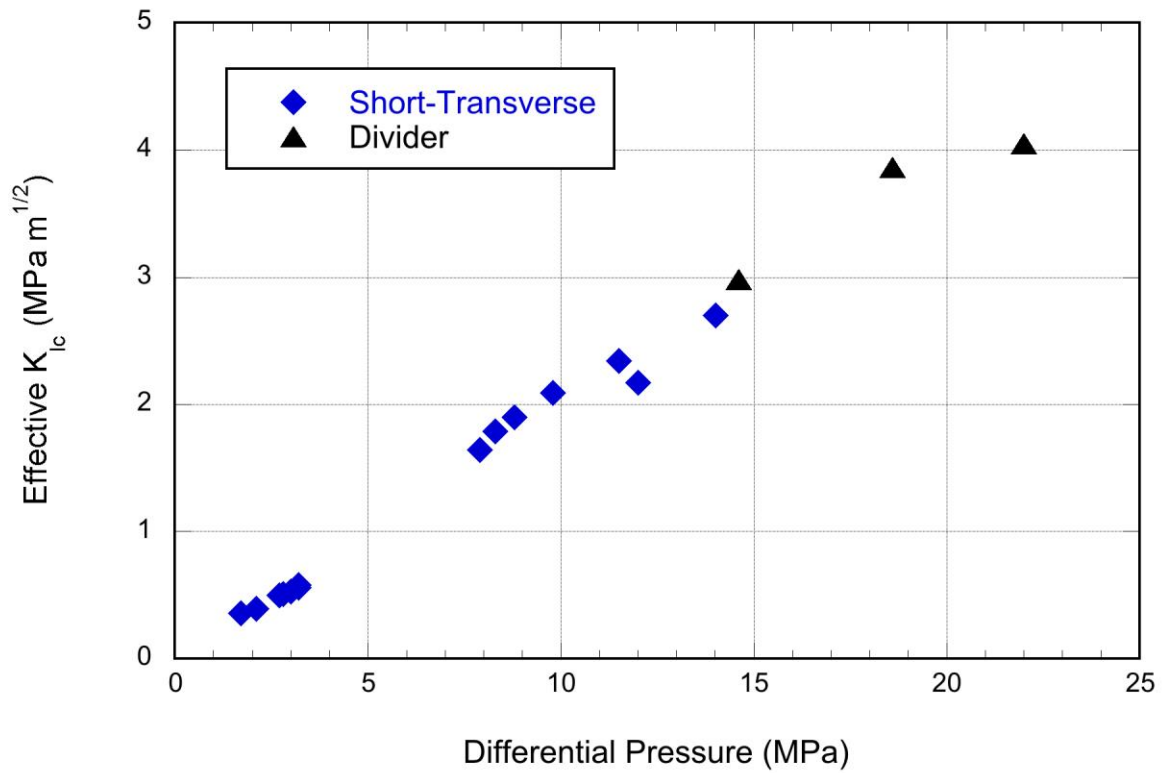
**Figure 7:** Variation in effective fracture toughness as a function of differential pressure for Nash Point shale. Data from tests on Short-Transverse samples are shown as blue diamonds and data from tests on Arrester samples are shown as black triangles.
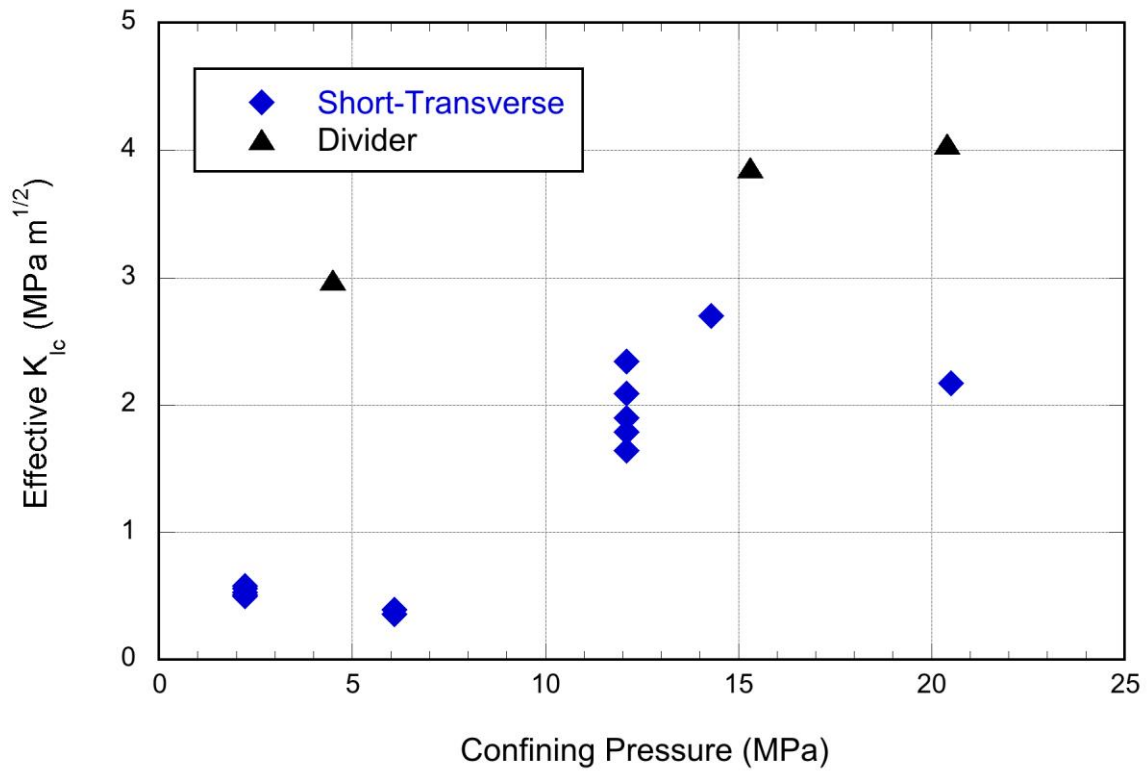
**Figure 8:** Variation in effective fracture toughness with confining pressure, determined from the fluid pressure oscillation and fracture growth cycles identified in Figure 5, for both Short-Transverse (blue diamonds) and Divider (black triangles) orientations.

Table 1: Calculations of effective fracture toughness ($eK_{Ic}$) as a function of confining pressure and fracture orientation from pressure oscillation analysis during hydraulic fracture experiments on samples of Nash Point shale. For each stage, "$a_f$" denotes the calculated crack length at the end of that stage, which then becomes the initial crack length for the following stage.

| Experiment | Confining Pressure (MPa) | Stage # | Differential Pressure (MPa) | $a_f$ (mm) | Fracture Toughness (MPa.m$^{1/2}$) |
|---|---|---|---|---|---|
| NPS-ST-2.2 | 2.21 | 1 | 3.20 | 5.25 | 0.58 |
| | | 2 | 3.20 | 5.55 | 0.56 |
| | | 3 | 3.00 | 5.74 | 0.53 |
| | | 4 | 2.80 | 5.94 | 0.51 |
| | | 5 | 2.70 | 6.16 | 0.50 |
| NPS-ST-6.1 | 6.10 | 1 | 2.10 | 6.37 | 0.39 |
| | | 2 | 1.70 | 13.60 | 0.36 |
| NPS-ST-12.1 | 12.10 | 1 | 11.50 | 11.73 | 2.34 |
| | | 2 | 9.80 | 12.81 | 2.09 |
| | | 3 | 8.80 | 13.11 | 1.90 |
| | | 4 | 8.30 | 13.35 | 1.79 |
| | | 5 | 7.90 | 13.55 | 1.64 |
| NPS-ST-14.3 | 14.30 | 1 | 14.01 | 10.98 | 2.76 |
| NPS-ST-20.5 | 20.50 | 1 | 12.00 | 7.03 | 2.17 |
| NPS-DIV-4.5 | 4.50 | 1 | 14.60 | 11.72 | 2.98 |
| NPS-DIV-15.3 | 15.30 | 1 | 18.60 | 12.22 | 3.86 |
| NPS-DIV-20.4 | 20.40 | 1 | 22.00 | 7.27 | 4.05 |

4